Inorganic Chemistry

pubs.acs.org/IC

Article

The Effects of Sr Content on the Performance of $Nd_{1-x}Sr_xCoO_{3-\delta}$ Air-Electrode Materials for Intermediate Temperature Solid Oxide Fuel Cells under Operational Conditions

Daniel Muñoz-Gil,* M. Teresa Azcondo, Clemens Ritter, Oscar Fabelo, Domingo Pérez-Coll, Glenn C. Mather, Ulises Amador, and Khalid Boulahya*

Cite This: https://dx.doi.org/10.1021/acs.inorgchem.0c01049

Read Online

ACCESS | Metrics & More | Article Recommendations | Supporting Information

ABSTRACT: The potential of the perovskite system $Nd_{1-x}Sr_xCoO_{3-\delta}$ (x = 1/3 and 2/3) as cathode material for solid oxide fuel cells (SOFCs) has been investigated via detailed structural, electrical, and electrochemical characterization. The average structure of x = 1/3 is orthorhombic with a complex microstructure consisting of intergrown, adjacent, perpendicularly oriented domains. This orthorhombic symmetry remains throughout the temperature range 373−1073 K, as observed by neutron powder diffraction. A higher Sr content of x = 2/3 leads to stabilization of the cubic perovskite with a homogeneous microstructure and with a higher oxygen vacancy content and cobalt oxidation state than the orthorhombic phase at SOFC operation temperature. Both materials are p-type electronic conductors with high total conductivities of 690 and 1675 S·cm^{-1} at 473 K in air for x = 1/3 and 2/3, respectively. Under working conditions, both compounds exhibit similar electronic conductivities, since x = 2/3 loses more oxygen on heating than x = 1/3, associated with a greater loss of p-type charger carriers. However, composite cathodes prepared with $Nd_{1/3}Sr_{2/3}CoO_{3-\delta}$ and $Ce_{0.8}Gd_{0.2}O_{2-\delta}$ present lower ASR values (0.10 Ω·cm^2 at 973 K in air) than composites prepared with $Nd_{2/3}Sr_{1/3}CoO_{3-\delta}$ and $Ce_{0.8}Gd_{0.2}O_{2-\delta}$ (0.34 Ω·cm^2). The high activity for the oxygen electrochemical reaction at intermediate temperatures is likely attributable to a large disordered oxygen-vacancy concentration, resulting in a very promising SOFC cathode for real devices.

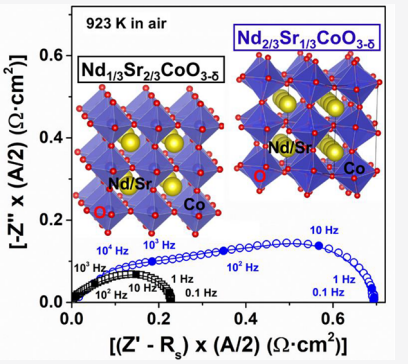

INTRODUCTION

The development of highly efficient energy conversion and storage devices plays a key role in addressing the current energy challenges of dwindling fossil-fuel supplies and increasing greenhouse−gas emissions. One of the most important goals at present is improving electrode materials for intermediate-temperature solid oxide fuel cells (IT-SOFCs).

Perovskite oxides (ABO_3) can accommodate both a large variety of metal ions with variable oxidation states and high concentrations of vacancies on the anionic sublattice.[1] These features render perovskites extremely important components of high-temperature electrochemical devices, including solid oxide fuel cells (SOFCs),[2−4] solid oxide electrolyzer cells (SOECs),[5,6] and oxygen-transport membranes.[7] Their applications range from state-of-the-art electrodes[8,9] (both cathodes and anodes) to electrolytes and interconnectors.

Air-electrode (cathode) materials in SOFCs require both mixed ionic-electronic conductivity (MIEC) and high catalytic activity for oxygen reduction.[10,11] Such properties are provided by cations in mixed oxidation states and mobile oxygen vacancies, which facilitate the interchange of oxygen under different oxygen partial pressures (pO_2).[12−16]

$La_{1-x}Sr_xMnO_3$ (LSM)[17] has been widely used as a cathode material for SOFCs, and, in more recent years, $La_{1-x}Sr_xCoO_3$ (LSC),[18,19] which displays higher catalytic activity than that of LSM. In general, cobalt-containing perovskites (cobaltites) exhibit a number of structural and physical properties which are desirable for the air electrode.[20] The presence of cobalt on the B site commonly results in oxides with high electronic conductivity, due both to the ability of cobalt to exist in different oxidations states ranging from II to IV and to the weak strength of the Co−O bond, which confers electron holes located at Co^{4+} species[21] with high mobility. Moreover, high oxide-ionic conductivity is expected for oxides with weak cation−oxygen bond strength,[22] in addition to imparting outstanding catalytic activity.[2,4,8,9,23,24]

Sr-doped lanthanide cobaltites, $Ln_{1-x}Sr_xCoO_{3-\delta}$ (Ln = Pr, Nd, Sm, and Gd), have been widely investigated as cathode

Received: April 9, 2020

materials for intermediate-temperature operation.[25−31] The oxide-ion vacancies impart both high ionic conductivity and excellent catalytic activity.[32] It has previously been reported that the $Ln_{1-x}Sr_xCoO_{3-\delta}$ (Ln = Nd, Sm, and Dy) systems react with $La_{0.8}Sr_{0.2}Ga_{0.8}Mg_{0.2}O_{2.8}$ (LSGM) and yttria-stabilized zirconia (YSZ) but show good stability with the electrolyte $Gd_{0.1}Ce_{0.9}O_{1.95}$ (GCO).[33−35] Sihyuk Choi et al. studied the structural properties of the $Nd_{1-x}Sr_xCoO_{3-\delta}$ system ($0.3 \leq x \leq 0.7$) using X-ray diffraction and determined the performances of an SOFC cathode on GCO at an intermediate temperature.[35] The average A-cation size is critical to the adopted symmetry, which may, in turn, impact on the electrochemical properties. $Sm_{1-x}Sr_xCoO_{3-\delta}$ and $Dy_{1-x}Sr_xCoO_{3-\delta}$ adopt cubic symmetry in the ranges x = 0.6−0.9 and x = 0.7−0.9, respectively,[26] whereas $Nd_{1-x}Sr_xCoO_{3-\delta}$ is reported to be orthorhombic over the complete substitution range ($0 \leq x \leq 1$).[33,35]

Here, we present a more complete understanding of the effects of the level of Sr substitution on the crystal structure (using neutron diffraction and transmission electron microscopy), cobalt oxidation state, oxygen-vacancy concentration, and electrical and electrochemical properties of the $Nd_{1-x}Sr_xCoO_{3-\delta}$ system with a view to its applications as a cathode for intermediate-temperature solid oxide fuel cells (IT-SOFCs).

EXPERIMENTAL SECTION

Polycrystalline samples of nominal composition $Nd_{1-x}Sr_xCoO_{3-\delta}$ (x = 1/3, 2/3) were prepared by heating stoichiometric amounts of $SrCO_3$ (Aldrich 99.98%), Co_3O_4 (Aldrich 99.9%), and Nd_2O_3 (Aldrich 99%) in air at 1373 K for 72 h with intermediate grindings, then slowly cooling to room temperature (RT).

Sample purity and structure were determined from powder X-ray diffraction (PXRD) data collected on a Bruker D8 high-resolution diffractometer equipped with a LynxEye fast detector using monochromatic Cu Kα_1 (λ = 1.5406 Å) radiation obtained with a germanium primary monochromator. The angular range, step size, and counting times were selected to ensure the required data quality and resolution for structural refinement. Diffraction data were analyzed using the Fullprof software.[36] The peak shape was described by a pseudo-Voigt function, and the background level was fitted by linear interpolation.

The chemical composition of the samples was semiquantitatively determined on sintered pellets by energy-dispersive X-ray spectroscopy (EDS) on an FEI XL30 scanning microscope using an EDAX detector; approximately 20 crystals of every sample were probed. This microscope was also used to determine the electrode morphology before and after polarization measurements.

The average oxidation state of cobalt and the oxygen content (assuming charge neutrality) of samples were determined by titration as described in the literature.[37] Thermogravimetric analyses (TGA) in air, performed using a Netzsch STA-409 PC-Luxx apparatus, provided information on the evolution of oxygen stoichiometry from RT to 973 K.

Neutron powder diffraction (NPD) patterns were recorded at RT on the high-resolution diffractometer D2B (ILL, Grenoble); a monochromatic beam of wavelength 1.050 Å was selected with a Ge monochromator from the primary beam. The instrumental resolution was increased by reducing the divergence of the primary beam by an additional 10′ collimator. The instrumental contribution to the line broadening was determined using a NIST standard sample of $Na_2Ca_3Al_2F_{14}$, whereas a standard sample of CeO_2 (also from NIST) was used for precise determination of the wavelength.

NPD patterns as a function of temperature from 373 to 1073 K in the air (in a quartz tube open to air) were collected on the D1B instrument at ILL, using a monochromatic beam of 1.280 Å. The contribution of the instrument to the peak width was determined by the instrument resolution function determined from a $Na_2Ca_3Al_2F_{14}$ standard sample, whereas the wavelength was determined using a Si standard.

Structural refinements from NPD data were performed by the Rietveld method using the FullProf software.[36] The neutron scattering amplitudes used in the Rietveld refinement were 0.7690, 0.7020, 0.2490, and 0.5803 ($\times 10^{-12}$ cm) for Nd^{3+}, Sr^{2+}, Co^{3+}, and O^{2-}, respectively; isotropic thermal factors (ITF) were employed for all atoms. Throughout the refinements, the perovskite A and B sites were constrained to be fully occupied, and a single thermal factor for all oxygen atoms was assumed.

The samples were further characterized by High Resolution Transmission Electron Microscopy (HRTEM) using a JEOL JEM-3000F electron microscope operated at 300 kV. Local composition was analyzed by EDS with an INCA Oxford analyzer system attached to the electron microscope.

Chemical compatibility of the title materials with $Ce_{0.9}Gd_{0.1}O_{2-\delta}$ (CGO, Fuel Cells Materials) was tested on heating mixtures of each compound with CGO (70:30 w/w) at 1173 K for 12 h followed by powder X-ray diffraction (PXRD) analysis.

Electrical conductivity was determined by the direct current (dc) four-probe method. Rectangular bars were prepared by pressing the powders and sintering at 1373 K for 8 h. The external surfaces of the bars were coated with Pt paste to ensure equipotential conditions. One pair of Pt wires was attached to the external surfaces, and another independent pair of Pt wires was internally located at a distance of ∼5 mm, with Pt paste. Good electrical contacts were assured after sintering at 1223 K for 1 h. Electrical characterization was performed by galvanostatic voltammetry using an Autolab PGSTAT302N potentiostat/galvanostat. Electrical current was applied through the external electrodes, and the voltage difference was measured between the inner electrodes. The electrical resistance of samples was obtained from the slopes of the I−V linear relationships in air and O_2 atmospheres in the temperature range 473−1223 K (gas-flow rates of 50 mL·min).

The electrochemical performance of the title oxides as cathodes in IT-SOFCs was evaluated by determination of area-specific resistance (ASR) at different temperatures in air by impedance spectroscopy (IS) on symmetrical two-electrode configuration cells. Electrolyte pellets of ∼8.6 mm diameter and ∼1 mm thickness of commercial CGO (Fuel Cells Materials) were prepared by pressing the powder at 250 MPa and sintering at 1773 K for 12 h (heating/cooling rate of 2.5 K·min^{-1}) in air. The composite cathode layers were painted onto the electrolyte with a brush. For this purpose, slurries consisting of composites of $Nd_{1-x}Sr_xCoO_{3-\delta}$:CGO (70:30 w/w) with x = 1/3 and 2/3, were prepared using Decoflux as a binder and deposited on both sides of the electrolyte pellets before firing at 1173 K for 3 h in air (heating/cooling rate of 2.5 K·min^{-1}). Silver paste and silver mesh were used as current collectors.

The IS data were collected in air on heating and cooling cycles between 773 and 973 K using a frequency response analyzer (Solartron 1255 + dielectric interface 1296) in the frequency range 0.1−10^6 Hz with an excitation voltage of 50 mV. The impedance spectra were fitted to equivalent circuits using the Zview software,[38] which allowed determination of the ohmic contributions, mainly ascribed to the electrolyte resistances, and the electrochemical contributions associated with the oxygen reaction at the electrodes.

RESULTS AND DISCUSSION

Phase Analysis and Cobalt Oxidation State. Samples of $Nd_{1-x}Sr_xCoO_{3-\delta}$ (x = 1/3, 2/3) prepared in air were single-phase at the resolution of PXRD. The metal compositions of both samples, determined by EDS, corresponded with the nominal compositions, within experimental error (Tables S1 and S2).

The cobalt oxidation state and the oxygen content, assuming electroneutrality, were determined by redox titration, giving

https://dx.doi.org/10.1021/acs.inorgchem.0c01049
Inorg. Chem. XXXX, XXX, XXX−XXX

the actual compositions as $Nd_{0.67}Sr_{0.33}CoO_{2.92(2)}$ ($Co^{+3.16(4)}$) and $Nd_{0.33}Sr_{0.67}CoO_{2.94(3)}$ ($Co^{+3.53(4)}$).

Room Temperature Crystal Structures. Profile fittings of the room temperature PXRD patterns were consistent with perovskite-like structures of different symmetries for $x = 1/3$ and 2/3 (Figure S1). The $(222)_p$ reflection of $Nd_{2/3}Sr_{1/3}CoO_{3-\delta}$ was split, indicating either orthorhombic symmetry with unit cell $2^{1/2}a_p \times 2a_p \times 2^{1/2}a_p$ (two peaks as in the inset of Figure S1a where a_p refers to the unit cell parameter of a cubic perovskite) or monoclinic with unit cell $2^{1/2}a_p \times 2^{1/2}a_p \times 2a_p$ and $\beta \approx 90°$ (three peaks, as previously observed for $Sr_{2-y}LuNb_{1-x}Ti_xO_6$ ($0 \le x \le 0.2$)).[39] However, systematic extinctions in the indexed pattern of $Nd_{2/3}Sr_{1/3}CoO_{3-\delta}$ (Figure S1a) were more consistent with orthorhombic symmetry (space group *Pnma*), in agreement with previous results.[33,35] This distortion of the perovskite is very common due to tilting of the BO_6 octahedra,[20,23] which accommodates the mismatch between the A-O and B−O bond distances.[1] In contrast, the pattern of $Nd_{1/3}Sr_{2/3}CoO_{3-\delta}$ suggested cubic symmetry with unit-cell dimensions $a_p \times a_p \times a_p$ as the $(222)_p$ peak was unsplit (Figure S1b). Since no systematic extinctions were observed, space group $Pm\bar{3}m$ (#221) was assumed, consistent with the aristotype of the family, where A−O and B−O bonds match and no tilting of the BO_6 octahedra occurs.

The HRTEM image of $Nd_{2/3}Sr_{1/3}CoO_{3-\delta}$ (Figure 1a) displays intergrown domains of highly ordered material oriented along the [010] and [10$\bar{1}$] directions. In domain A, *d* spacings of 5.3 and 5.4 Å in perpendicular directions corresponding to d_{100} and d_{001} (indexed on the basis of the $\sqrt{2}a_p \times 2a_p \times \sqrt{2}a_p$ cell) are observed, consistent with the orthorhombic cell determined by PXRD. Domain B (Figure 1a) exhibits perpendicular spacing corresponding to d_{010} (double-perovskite axis) and the primitive perovskite axis d_{101}. Fast Fourier Transformation (FFT) of both domains confirms the absence of any short-range ordering.

In contrast, the HTREM image of $Nd_{1/3}Sr_{2/3}CoO_{3-\delta}$ (Figure 1b), taken along [001], reveals a well-ordered material with *d* spacings of 3.8 Å in perpendicular directions corresponding to d_{010} and d_{100}. FFT of the micrograph (see inset of Figure 1b) indicated that the crystal is homogeneous since the only maxima observed correspond to the simple cubic cell.

We note that the systematic extinctions of space group *Pnma* determined by PXRD (and confirmed by NPD) are not observed in these FFT images, most likely due to double diffraction arising from the complex microstructure.

The Goldsmith tolerance factor, *t*, is widely used to predict the symmetry of perovskites:[1]

$$t = (r_A + r_O)/(r_B + r_O) \quad (1)$$

where r_A, r_B, and r_O are the radii of A, B, and oxide ions, respectively.[40]

For the title materials, r_A is the weighted average ionic radius of Nd^{3+} and Sr^{2+} cations ($^{XII}r(Nd^{3+}) = 1.27$ Å; $^{XII}r(Sr^{2+}) = 1.44$ Å) and $^{VI}r(O^{2-}) = 1.40$ Å. The assignment of a radius to cobalt is much more problematic since it is present in two oxidation states, Co(III) and Co(IV) of different sizes (as determined by redox titration and confirmed by NPD, see below). Moreover, both trivalent and tetravalent cobalt in octahedral coordination may be present in different spin states (HS, IS, and LS) of varying radii.[40] The values of *t*, computed using these radii and the oxidation state of cobalt determined from redox titration,

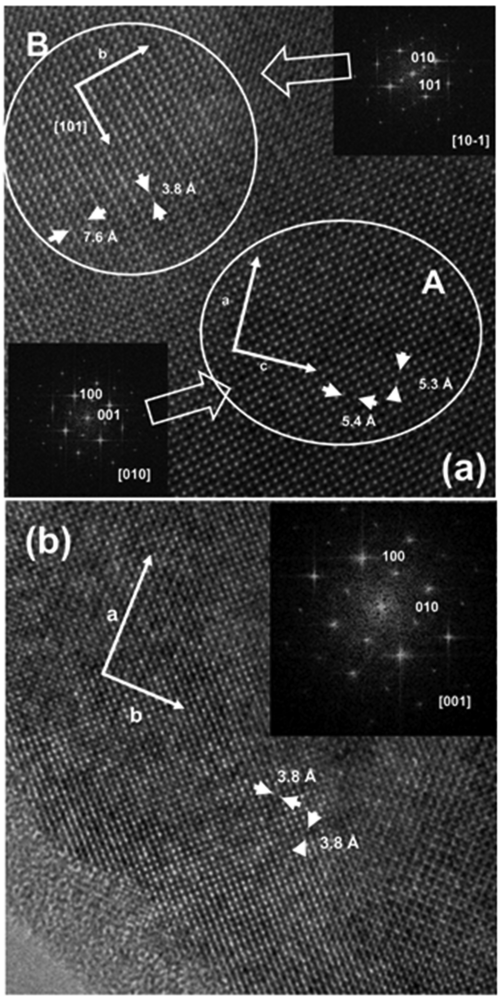

Figure 1. (a) HRTEM image of $Nd_{2/3}Sr_{1/3}CoO_{3-\delta}$ showing two types of intergrown domains, A oriented along [010] and B oriented along [10$\bar{1}$]. The insets display the corresponding FFT patterns. (b) HRTEM image of $Nd_{1/3}Sr_{2/3}CoO_{3-\delta}$ taken along the [001] direction; the inset displays the corresponding FFT pattern.

are in the ranges 0.985−0.958 and 1.011−0.998, depending on the proportion of LS and HS Co^{3+}, for the $x = 1/3$ and 2/3 oxides, respectively. A value of *t* close to unity suggests cubic symmetry, whereas a lower value is associated with lower symmetry, as is the case of orthorhombic $Nd_{2/3}Sr_{1/3}CoO_{3-\delta}$.

Structural models of the $x = 1/3$ and 2/3 perovskites in space groups *Pnma* and $Pm\bar{3}m$, respectively, were refined to fit the corresponding NPD patterns; Figure 2a and b show the observed and calculated NPD patterns and their difference for each phase. Final refined structural parameters and selected structural information are provided in Tables S3 and S4, respectively.

The tilting angles of the CoO_6 octahedra of $Nd_{2/3}Sr_{1/3}CoO_{3-\delta}$ (Table S4) are moderate, consistent with an orthorhombically distorted perovskite with a relatively minor mismatch of A−O and B−O bonds and a tolerance factor close to unity. The cation composition corresponds approximately to the nominal stoichiometry, as determined by EDS, and the oxygen content is consistent with that obtained by chemical titration. The values of the bond-valence sum (BVS) for Co should be approached with caution (due to the difficulty in defining a Co^{3+}−O distance) but nevertheless indicate, along with the lower volume of the CoO_6 octahedra

https://dx.doi.org/10.1021/acs.inorgchem.0c01049
Inorg. Chem. XXXX, XXX, XXX−XXX

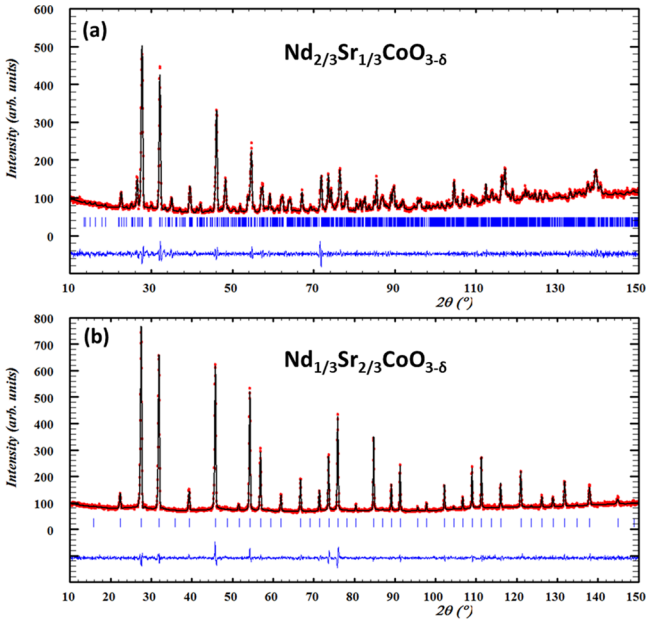

Figure 2. Experimental (red points), calculated (solid black line) and difference (blue line at bottom) NPD patterns at RT for $Nd_{2/3}Sr_{1/3}CoO_{3-\delta}$ (a) and $Nd_{1/3}Sr_{2/3}CoO_{3-\delta}$ (b); vertical bars indicate the expected position of Bragg peaks.

and shorter Co−O distances, that the oxidation state of Co is higher in the $x = 2/3$ phase than in $x = 1/3$. In the former cubic composition, the A−O and B−O distances result in a tolerance factor of exactly one.

Evolution of the Structures and Compositions with Temperature. To correlate the physical properties with the crystal structure under operating conditions, an in-depth study of the structure and oxygen content was carried out employing neutron powder diffraction as a function of temperature in the range 373−1073 K.

As mentioned earlier, $Nd_{2/3}Sr_{1/3}CoO_{3-\delta}$ presents an orthorhombic structure (space group, *Pnma*) due to tilting of the octahedra following the scheme ($a^-b^+a^-$) in Glazer notation[41] (corresponding to a unit cell $\sqrt{2}a_p \times 2a_p \times \sqrt{2}a_p$). Accordingly, two consecutive octahedra are equally tilted out-of-phase in opposite directions along two Cartesian directions of the cubic perovskite, and the octahedra are tilted in-phase in the third direction (in this case, corresponding to the $2a_p$ axis) by a different angle from that adopted in the other two directions. In contrast, in the cubic structure the octahedra are not tilted.

It is very common for perovskites to undergo phase transitions driven by different thermodynamic parameters, mainly temperature and pressure (internal or external), which cause changes in the magnitude and type of octahedral tilting.[42−45] However, the NPD patterns clearly demonstrated that $Nd_{2/3}Sr_{1/3}O_{3-\delta}$ retains the *Pnma* symmetry when heated at 1073 K in air since the observed (122) and (221) peaks are not compatible with space groups *Imma* or $R\bar{3}c$ (Figure 3).

The thermal evolution of the tilting angles of $Nd_{2/3}Sr_{1/3}CoO_{3-\delta}$ is plotted in Figure 4. The symmetry of perovskites commonly evolves on heating through different sequences, such as

Pnma → *Imma* → $R\bar{3}c$ → $Pm\bar{3}m$, e.g., $BaPrO_3$[46−48]
Pnma → *Imma* → *I4/mcm* → $Pm\bar{3}m$, e.g., $SrZrO_3$[49]
Pnma → $R\bar{3}c$ → $Pm\bar{3}m$, e.g., $La_{1.5}Sr_{0.5}CoTiO_{6-\delta}$[42]

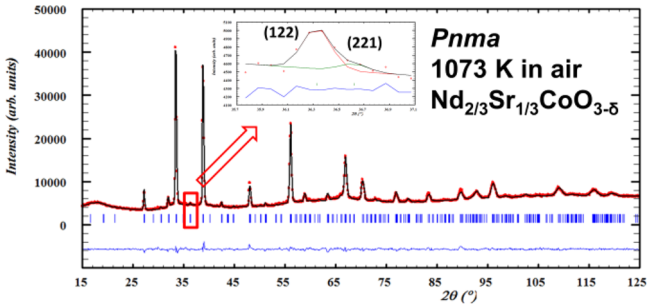

Figure 3. Experimental (red points), calculated (solid black line), and difference (blue line at bottom) NPD patterns at 1073 K in air for $Nd_{2/3}Sr_{1/3}CoO_{3-\delta}$; vertical bars indicate the expected position of Bragg peaks.

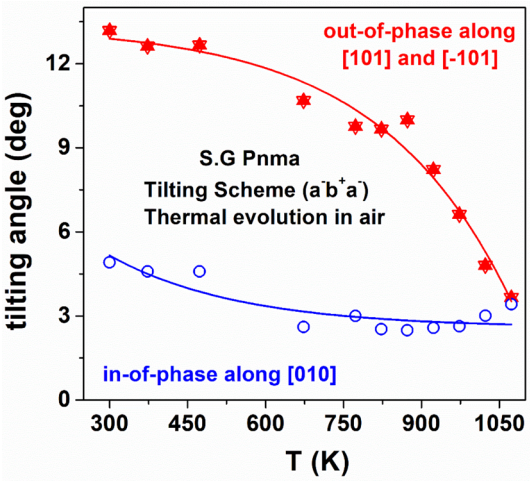

Figure 4. Thermal evolution of the octahedral tilting angles in orthorhombic $Nd_{2/3}Sr_{1/3}O_{3-\delta}$ in the air. Solid red triangles along [101], inverted open red triangles along [$\bar{1}$01] and open blue circles along [010].

The transformation from *Pnma* symmetry ($a^-b^+a^-$) to either *Imma* ($a^-b^0a^-$) or $R\bar{3}c$ ($a^-a^-a^-$) symmetries is a first-order transition with discontinuity in the first derivatives of the free energy. At the transition temperature, the in-phase tilt angle either vanishes (S.G., *Imma*) or reorientates and changes its sign (to $R\bar{3}c$). As shown in Figure 4, neither of these effects is observed since the in-phase angle decreases slightly. Thus, although the distortion associated with the octahedra tilting is thermally alleviated, the $Nd_{2/3}Sr_{1/3}CoO_{3-\delta}$ perovskite retains the orthorhombic structure with *Pnma* symmetry and tilting scheme ($a^-b^+a^-$) up to 1073 K.

Figure S2a shows the evolution of the unit-cell volume of $Nd_{2/3}Sr_{1/3}CoO_{3-\delta}$ as a function of temperature on heating; two different linear regimes are exhibited, with greater expansion at higher temperature, rather than a single linear dependence. A volume TEC may be obtained from these values, and although the structure is anisotropic, a linear TEC can be calculated to be in the range $(15-25) \times 10^{-6}$ K^{-1}, with a significant increment in the high-temperature range.

On the other hand, $Nd_{1/3}Sr_{2/3}CoO_{3-\delta}$ presents a simple cubic perovskite structure at RT, as discussed above. Although heating results in cell expansion and oxygen loss, the neutron thermo-diffraction data indicate that the cubic structure is retained throughout the measured temperature range, as expected (Figure S3). Figure S2b displays a nonlinear

https://dx.doi.org/10.1021/acs.inorgchem.0c01049
Inorg. Chem. XXXX, XXX, XXX−XXX

dependence of cell volume with temperature, probably due to oxygen loss on heating. As reported for previous perovskite cobaltites,[9,46] the linear TEC for this oxide is rather high, in the range of (15−30) × 10^{-6} K^{-1}, even higher than for the orthorhombic phase. These high TEC values for both oxides must be related not only to the well-known magnetic transition of cobalt ions[46,47] but also to cobalt reduction associated with oxygen loss (Figure S4).

Different strategies can be used to reduce the TEC of these kinds of cobaltites. For example, adding electrolyte materials to form cathode composites has been demonstrated to be an effective way to reduce the TEC.[50−54] For this reason, in the present article, we have studied the electrochemical behavior of the $Nd_{1-x}Sr_xCoO_{3-\delta}$ system as a cathode for IT-SOFC using a composite cathode ($Nd_{1-x}Sr_xCoO_{3-\delta}$:CGO 70:30 w/w) instead of using only $Nd_{1-x}Sr_xCoO_{3-\delta}$, with the aim of reducing the TEC, which also leads to improved contact at the cathode/electrolyte interface. Another strategy may consist in improving the efficiency of the electrode in the lower-temperature range, where the corresponding TEC is closer to that of the electrolyte. The use of suitable active interlayers has been demonstrated recently to be an effective way to improve the electrochemical performance of perovskite cathodes in the lower temperature range.[55]

The oxygen loss is much less pronounced in $Nd_{2/3}Sr_{1/3}CoO_{3-\delta}$ (see Figure S4); thus, its TEC at high temperature is also lower. In addition to the lower oxygen loss for $Nd_{2/3}Sr_{1/3}CoO_{3-\delta}$, this effect begins at higher temperature (~800 K) compared with $Nd_{1/3}Sr_{2/3}CoO_{3-\delta}$ (~650 K; Figure S4); the oxygen content of $Nd_{2/3}Sr_{1/3}CoO_{3-\delta}$ (2.89) is, therefore, higher than that of $Nd_{1/3}Sr_{2/3}CoO_{3-\delta}$ (2.81), at the SOFC operating temperature of 973 K. Figure 5 shows the evolution of the oxygen content and the oxidation state of cobalt as a function of temperature for x = 1/3 and 2/3, determined from the results of NPD. Although $Nd_{2/3}Sr_{1/3}CoO_{3-\delta}$ exhibits a lower concentration of oxygen vacancies at 973 K, its cobalt oxidation state (~3.12) is significantly lower than in the cubic perovskite $Nd_{1/3}Sr_{2/3}CoO_{3-\delta}$ (~3.28) at the same temperature.

Although the as-prepared x = 2/3 compound is slightly oxygen deficient, oxygen loss begins at a temperature as low as 573 K (in agreement with TGA results shown in Figure S4b), reaching a significant content of oxygen vacancies at 973 K (δ ~ 0.20) with a quite high cobalt oxidation state (~3.28, suggesting that about 28% of cobalt is in the tetravalent oxidation state). Both features are important for understanding the electrical and electrochemical properties of this oxide in comparison with the x = 1/3 member of the $Nd_{1-x}Sr_xCoO_{3-\delta}$ series, as discussed below.

Chemical Stability and Compatibility with Electrolyte. The chemical stability (oxygen loss and uptake) and compatibility of the title compounds with the electrolyte composition (CGO) were evaluated under simulated processing and working conditions. Figure S4a shows that $Nd_{2/3}Sr_{1/3}CoO_{2.92(2)}$ loses a small amount of oxygen when heated in air to 973 K, where the oxygen content is 2.89, which corresponds to a cobalt oxidation state of $Co^{+3.12}$. On the other hand, the $Nd_{1/3}Sr_{2/3}CoO_{2.94(3)}$ phase loses much more weight under the same conditions (Figure S4b), reaching a final oxygen stoichiometry of 2.81 at 973 K, which implies a cobalt oxidation state of $Co^{+3.28}$, well above the trivalent state.

The PXRD patterns of cathode composites of $Nd_{1-x}Sr_xCoO_{3-\delta}$:CGO (70:30; w/w) heated for 48 h at 1173 K, in Figure 6, only show Bragg maxima corresponding to the perovskites and CGO, suggesting negligible decomposition and good long-term stability.

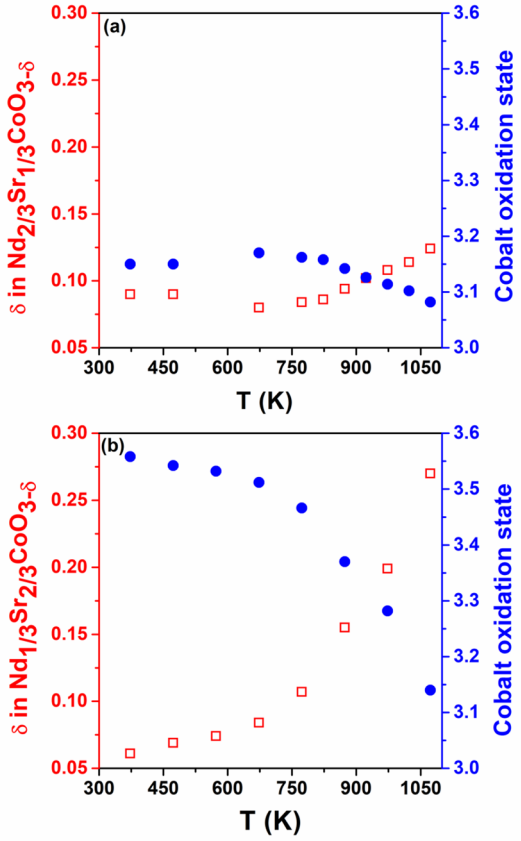

Figure 5. Thermal evolution of the oxygen content and cobalt oxidation state for (a) orthorhombic $Nd_{2/3}Sr_{1/3}O_{3-\delta}$ and (b) cubic $Nd_{1/3}Sr_{2/3}O_{3-\delta}$ in air, determined from NPD.

Electrical Conductivity. The temperature dependence of electrical conductivity of the title compounds is shown in Figure 7 under air and O_2 atmospheres. Conductivities as high as 1675 and 1885 S·cm^{-1} are observed for the sample x = 2/3 at 473 K in air and O_2, respectively. Although x = 1/3 presents much lower values under the same conditions, 690 and 810 S·cm^{-1} in air and O_2, respectively, they are, nevertheless, in the high range expected for perovskite cobaltites. The very weak strength of the Co−O bonds is likely to be responsible for the high mobility of electron holes, located at Co^{4+} species.[21]

This large difference in conductivity observed between the two compositions should be attributable to different p-type carrier concentrations associated with the average Co-oxidation states determined by redox titration at room temperature of 3.16 and 3.53 for $Nd_{2/3}Sr_{1/3}CoO_{2.92(2)}$ and $Nd_{1/3}Sr_{2/3}CoO_{2.94(3)}$, respectively. However, as the temperature increases, the conductivity of sample x = 2/3 decreases monotonically, leading to values of ~460 and 600 S·cm^{-1} at 973 K in air and O_2, respectively. This decrease corresponds to the significant oxygen loss observed by thermogravimetric analysis, shown in Figure S4b, leading to the elimination of electron holes via the reduction of Co^{4+} species to Co^{3+}. The electrical behavior of the sample with x = 1/3 is different in the low-temperature range, slightly increasing as the temperature is raised to ~623 K, then decreasing at higher temperature due to the mass loss corresponding to the creation of oxygen

https://dx.doi.org/10.1021/acs.inorgchem.0c01049
Inorg. Chem. XXXX, XXX, XXX−XXX

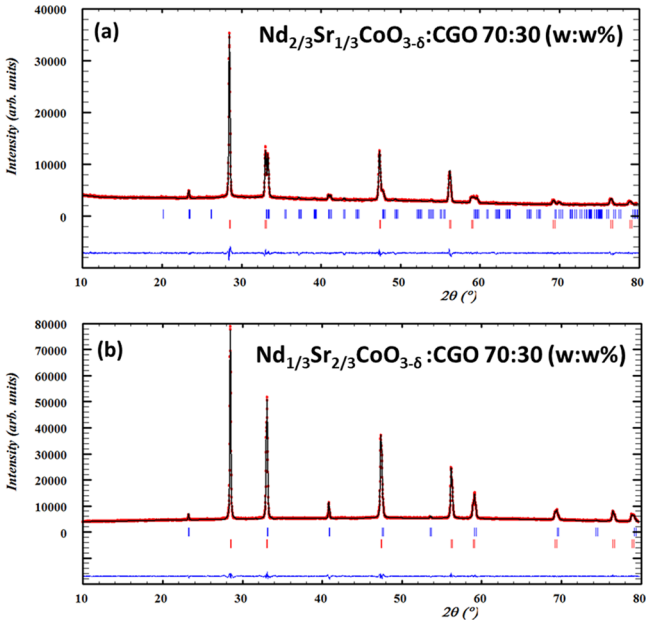

Figure 6. LeBail fitting of PXRD patterns of composites (70:30 w/w) of (a) $Nd_{2/3}Sr_{1/3}CoO_{3-\delta}$:CGO and (b) $Nd_{1/3}Sr_{2/3}CoO_{3-\delta}$:CGO, treated in air for 48 h at 1173 K. The first row of vertical bars indicates the positions of Bragg reflections of the perovskite and the second row those of CGO.

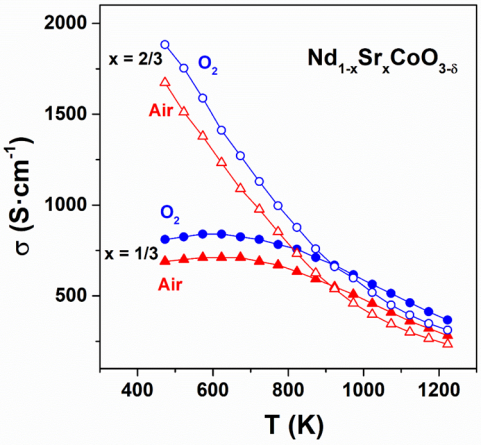

Figure 7. Electrical conductivity as a function of temperature for $Nd_{1-x}Sr_xO_{3-\delta}$ (x = 1/3, 2/3) in air and O_2.

vacancies and reduction of the electron−hole content. It is also expected that the significant oxygen loss of the x = 2/3 composition further decreases the electron- hole mobility, as a consequence of the lower concentration of Co−O−Co bonds and the corresponding expansion associated with the creation of oxygen vacancies.[56−58] Note that the onsets of mass loss and drop in conductivity do not occur at the same temperature in the TGA and electrical measurements. This may be attributable to the dynamic nature of TGA, which is expected to displace observance of the mass loss to a higher temperature.

Polarization Test on Symmetrical Cells. Figure 8 shows Nyquist impedance plots of symmetrical cells based on the configuration $Nd_{1-x}Sr_xCoO_{3-\delta}$:CGO (70:30 w/w):CGO/ $Nd_{1-x}Sr_xCoO_{3-\delta}$:CGO (70:30 w/w). The data were fitted to the equivalent circuit shown in the inset of Figure 8 to separate

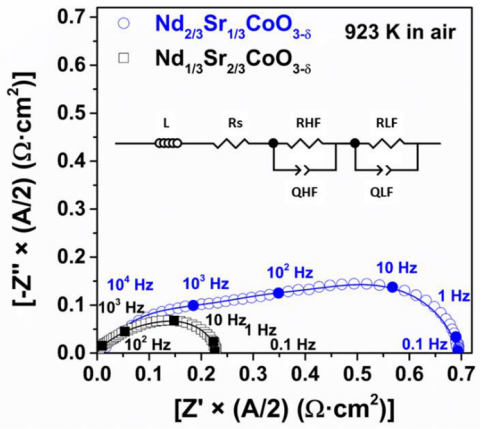

Figure 8. Impedance spectra measured at 923 K in air on symmetrical cells with $Nd_{2/3}Sr_{1/3}CoO_{3-\delta}$ (blue circles) and $Nd_{1/3}Sr_{2/3}CoO_{3-\delta}$ (black squares). The inset shows the equivalent circuit used to fit the spectra (the solid lines represent spectra calculated using the equivalent circuit).

the different contributions and determine the area-specific resistance (ASR) values associated with the electrochemical process. The model consists of an inductance (L) caused by the experimental setup, a series resistance (Rs) to account for the ohmic contribution, mainly ascribed to the electrolyte, and two serial RQ elements associated with the electrochemical processes at the electrodes (R = resistance, Q = constant phase element with impedance $Q^{-1}(i\omega)^{-n}$, where the exponent n lies in the range $0 \leq n \leq 1$; for an ideal capacitor, $n = 1$). Note that the spectra have been displaced to the origin of the real axis for a clearer comparison of the electrode contributions. From the (RQ) values, the capacitance (C) and the relaxation frequency (f) may be calculated using expressions 2, 3, and 4:

$$C = \frac{(RQ)^{1/n}}{R} \tag{2}$$

$$f = \frac{\omega}{2\pi} \tag{3}$$

$$\omega = (RQ)^{-1/n} \tag{4}$$

In mixed ionic-electronic conducting cathode materials, three different possible paths for the electrochemical reaction may be considered:[59] (i) the electrode-surface path, where oxygen is adsorbed at the cathode surface and diffuses toward the triple-phase boundary (TPB); (ii) the bulk path, where the oxygen species are incorporated into the cathode and diffuse through the bulk electrode; (iii) the electrolyte-surface path, where the adsorption and diffusion of oxygen toward the TPB occur at the surface of the electrolyte. The electrochemical behavior of mixed-conducting cathodes with fast ionic transport is considered to be determined by exchange of oxygen at the surface and oxygen diffusion in the bulk of the cathode.[10,60] In this treatment, the bulk path dominates the cathodic reaction in electrode materials with high ionic conductivity and is composed of various steps, including diffusion, adsorption, and dissociation of oxygen molecules at the surface, followed by ionization, then the incorporation and diffusion of oxide ions through the cathode and transfer to the electrolyte.[59]

Given that paths i−iii are likely to occur simultaneously in the electrochemical process, the overall reaction rate is

https://dx.doi.org/10.1021/acs.inorgchem.0c01049
Inorg. Chem. XXXX, XXX, XXX−XXX

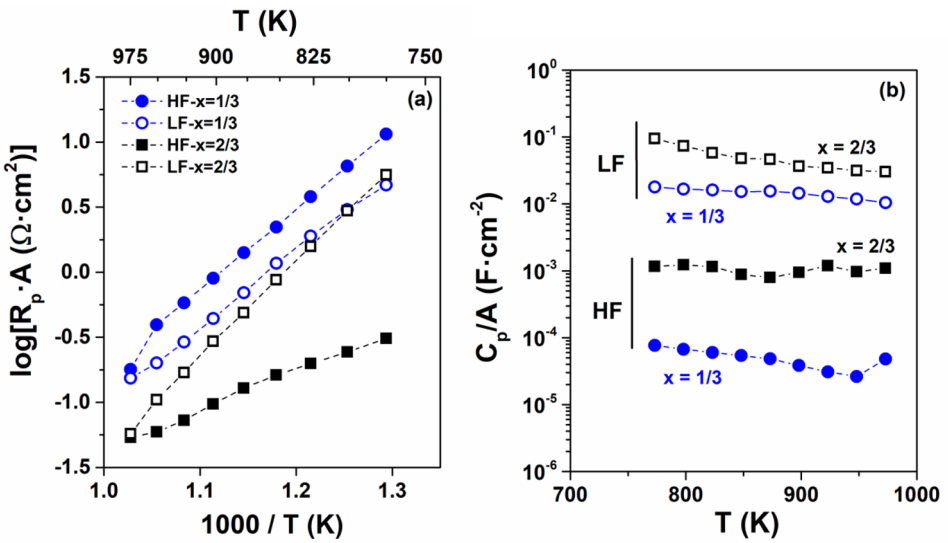

Figure 9. Temperature dependence of electrochemical resistance (a) and capacitance (b) associated with the high-frequency and low-frequency processes of the impedance spectra for composite $Nd_{1-x}Sr_xCoO_{3-\delta}$:CGO cathodes on CGO electrolyte.

determined by the fastest rate-determining step.[59] In porous cathode materials, with no gas-diffusion limitations, it was argued that the low-frequency contribution in the impedance spectra is expected to be associated with reactions at the surface, whereas the high-frequency contribution should be mainly determined by the diffusion of oxygen ions through the mixed-conducting material.[61] All the impedance spectra of the composites can be fitted with two RQ contributions.

The area-specific resistance of the low-frequency contribution is similar for both phases in the low-temperature range but is lower for $x = 2/3$ with respect to $x = 1/3$ at a higher temperature (Figure 9a). In the low-frequency range, both materials exhibit capacitances around 10^{-2} F cm^{-2}. The high-frequency contribution displays capacitance values around 10^{-5} to 10^{-4} and 10^{-3} F/cm^2 for $x = 1/3$ and $x = 2/3$ compositions, respectively (Figure 9b); however, the associated area specific resistance of this contribution is between 1 and 2 orders of magnitude lower for $x = 2/3$ compared to $x = 1/3$ (Figure 9a).

As mentioned before, the high-frequency contribution is expected to be dominated by bulk oxide-ion diffusion, whereas the low-frequency contribution should be limited by the surface exchange kinetics.[61] Note that, although at low temperature, the electronic conductivity of the $x = 2/3$ compound is clearly higher than that of $x = 1/3$, at SOFC working temperatures, both materials present similar electronic contributions. In this regard, it is expected that, in mixed-conducting cathodes, oxygen vacancies are the determinant species in the oxygen reduction reaction. They are considered to act as sinks for oxygen incorporation, facilitating electrocatalysis and enhancing oxygen bulk diffusion.[62] In other words, the vacancies are key to both fast surface exchange and high diffusion through the bulk. In support of this hypothesis, a linear relation between surface exchange constant and oxygen diffusion coefficient has been found in "electron-rich" perovskites typically employed as cathodes in SOFCs.[63]

The introduction of Sr in $Nd_{1-x}Sr_xCoO_{3-\delta}$ stabilized cubic symmetry for $x = 2/3$, whereas the orthorhombic symmetry is retained for $x = 1/3$ in the 300−1073 K temperature range. Moreover, although the oxygen content, determined by titration, is slightly higher at room temperature for the sample $x = 2/3$ in comparison to $x = 1/3$, the significant oxygen release of the former as temperature rises produces a higher concentration of oxygen vacancies at working temperatures (Figure S4 and Figure 5). These features suggest that oxide-ion transport is likely to be greater in the $x = 2/3$ sample. This agrees well with expected higher oxide-ion diffusion in the mixed conducting electrode and enhanced oxygen exchange kinetics for the $x = 2/3$ composition as temperature rises, which is reflected in the lower values of electrode polarization resistance for the high-frequency and low-frequency components, respectively (Figure 9a).

Figure 10 displays the effect of temperature on the total area-specific electrode polarization resistance for both materials. Similar results were obtained during both heating and cooling cycles, revealing noticeably lower ASR values for $Nd_{1/3}Sr_{2/3}CoO_{3-\delta}$ compared to $Nd_{2/3}Sr_{1/3}CoO_{3-\delta}$, as a consequence of the improved performance associated with

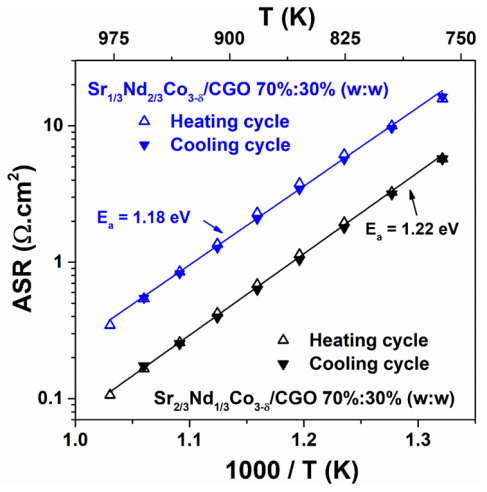

Figure 10. Arrhenius plot of the area-specific resistance (ASR) obtained from the impedance spectra of symmetrical cells with configuration $Nd_{2/3}Sr_{1/3}CoO_{3-\delta}$:CGO/CGO/$Nd_{2/3}Sr_{1/3}CoO_{3-\delta}$:CGO (solid blue symbols) and $Nd_{1/3}Sr_{2/3}CoO_{3-\delta}$:CGO/CGO/$Nd_{1/3}Sr_{2/3}CoO_{3-\delta}$:CGO (open black symbols) on heating (triangles) and cooling (inverted triangles) in air.

https://dx.doi.org/10.1021/acs.inorgchem.0c01049
Inorg. Chem. XXXX, XXX, XXX−XXX

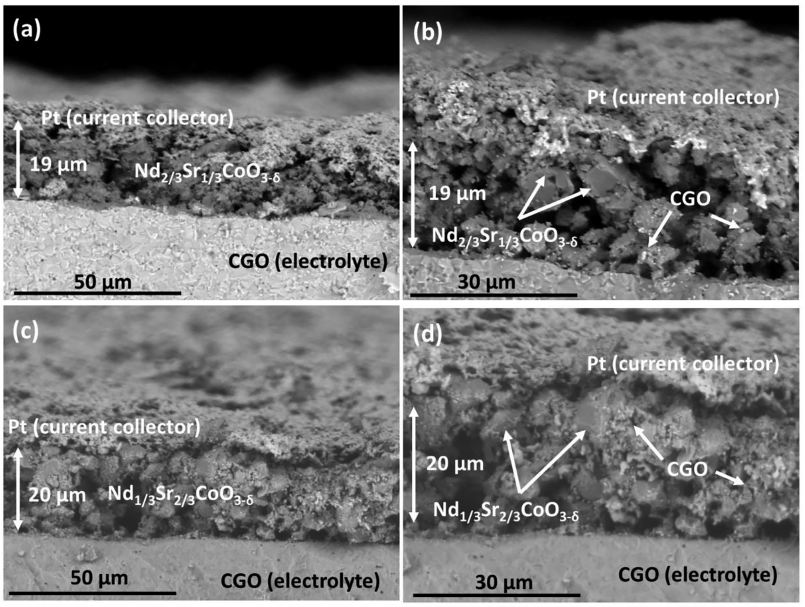

Figure 11. Cross section of symmetrical electrodes composed of (a,b) CGO-$Nd_{2/3}Sr_{1/3}CoO_{3-\delta}$ and (c,d) CGO-$Nd_{1/3}Sr_{2/3}CoO_{3-\delta}$ composites taken at different magnifications. Left panels (a−c) show a general view and right panels (b−d) show a detailed view revealing two kinds of particles corresponding to the different components of the electrode.

improved surface exchange kinetics and oxide-ion diffusion. Values of ASR as low as 0.10 Ω·cm^2 and 0.22 Ω·cm^2 were obtained in air for x = 2/3 at 973 and 923 K, respectively, whereas the corresponding values increased to 0.34 Ω·cm^2 and 0.70 Ω·cm^2 for x = 1/3 under the same working conditions. Similar values of area specific resistance have been reported earlier for $Nd_{1-x}Sr_xCoO_{3-\delta}$.[35] On the other hand, the total activation energies for both samples are essentially the same (1.18 and 1.22 eV), suggesting similar dependence of the limiting electrochemical processes with temperature.

Impedance spectroscopy was also performed for samples prepared with porous Pt instead of Ag as current collector, to analyze the possible influence of the porous metal layer on the electrochemical performance. Similar values of area specific resistance were obtained regardless of the employed porous metal layer, suggesting that the main role of both components is related to current collection. This also follows from the SEM images (Figure 11), where the current collector is only present at the top surface, not through the volume of the cathode materials where the electrochemical reactions take place, due to the mixed-conducting character of the electrode components.

The significant difference in the ASR values between x = 1/3 and x = 2/3 in $Nd_{1-x}Sr_xCoO_{3-\delta}$ is likely to be related, therefore, with the stabilization of the cubic perovskite and a higher concentration of oxygen vacancies at high temperature and, in turn, better electrocatalytic activity. In this regard, the electrochemical reaction includes reduction of oxygen gas to ions, and their incorporation and diffusion through the lattice, requiring high values of both electronic and oxide-ionic conductivity.[64]

Figure 11 shows the cross-section corresponding to the electrode/electrolyte interface for the phases $Nd_{2/3}Sr_{1/3}CoO_{3-\delta}$ and $Nd_{1/3}Sr_{2/3}CoO_{3-\delta}$ at different magnifications. The figures on the left (Figure 11a and c) display a general view, where we can see the porosity of the electrodes. In addition, the thickness of the electrode is around 20 μm for both samples, showing good interface contact between the electrolyte and the electrode. The figures on the right (at higher magnification) show with more detail the microstructure of the electrodes (Figure 11b and d). Given that a composite between $Nd_{1-x}Sr_xCoO_{3-\delta}$ and CGO was used as an electrode, two different kind of particles with different sizes and morphologies were found. The largest particles correspond to $Nd_{1-x}Sr_xCoO_{3-\delta}$ and the much smaller particles to CGO.

The behavior of the title oxides as cathode components has been determined on composites prepared without performing any microstructural optimization. As mentioned in the Experimental Section, the studied compositions were prepared by solid state reaction, leading to powders with large grain sizes. Therefore, it is expected that an improved performance may be obtained by using a more advanced synthesis route in which the microstructure are optimized. In addition, improving the deposition methodology by means of spin coating, screen-printing, or spray pyrolysis may also contribute to enhancing the electrochemical behavior.

CONCLUSIONS

In contrast to previous literature reports, the system $Nd_{1-x}Sr_xCoO_3$ does not adopt orthorhombic symmetry over the whole range of x, as verified by neutron powder diffraction. In accordance with tolerance-factor guidelines, a higher Sr content in the $Nd_{1-x}Sr_xCoO_{3-\delta}$ series stabilizes the cubic perovskite phase ($a_p \times a_p \times a_p$, S.G. $Pm\bar{3}m$) for x = 2/3. In contrast, $Nd_{2/3}Sr_{1/3}CoO_{3-\delta}$ exhibits orthorhombic symmetry with a diagonal unit cell ($2^{1/2}a_p \times 2a_p \times 2^{1/2}a_p$, S.G. *Pnma*) and maintains this symmetry throughout the temperature range 373−1073 K. The orthorhombic phase presents a much more complex microstructure of adjacent, perpendicularly oriented domains, whereas the cubic compound exhibits a homogeneous microstructure.

In both compositions, the room-temperature cobalt oxidation state is higher than +3, even in the presence of a relatively large concentration of oxygen vacancies: $Nd_{2/3}Sr_{1/3}CoO_{2.92(2)}$ ($Co^{+3.16(4)}$) and $Nd_{1/3}Sr_{2/3}CoO_{2.94(3)}$

https://dx.doi.org/10.1021/acs.inorgchem.0c01049
Inorg. Chem. XXXX, XXX, XXX−XXX

($Co^{+3.53(4)}$). The mixed valence states, the high cobalt oxidation state, and high oxide-ion-vacancy content exert a crucial influence on the electrical and electrochemical properties. Both phases are predominantly p-type electronic conductors with high total conductivities in oxidizing atmospheres. At low temperature (~500 K), the total conductivity of $Nd_{1/3}Sr_{2/3}CoO_{3-\delta}$ is more than twice that of $Nd_{2/3}Sr_{1/3}CoO_{3-\delta}$. However, at SOFC operating temperatures (800−1100 K), the conductivity is similarly high for both compositions due to the faster rate of oxygen loss for $Nd_{1/3}Sr_{2/3}CoO_{3-\delta}$ on heating, concomitant with the annihilation of p-type charge carriers and lower mobility, leading to a significant decrease of conductivity. Nevertheless, composite cathodes prepared with $Nd_{1/3}Sr_{2/3}CoO_{3-\delta}$ exhibit lower ASR values, most likely due to the stabilization of the cubic perovskite and its higher concentration of oxygen vacancies at high temperatures, which improves the activity for oxygen reduction. The excellent electrochemical performance of this material is very promising for its application as an SOFC cathode in real devices.

■ ASSOCIATED CONTENT

Supporting Information

The Supporting Information is available free of charge at https://pubs.acs.org/doi/10.1021/acs.inorgchem.0c01049.

(Figure S1) PXRD patterns $Nd_{2/3}Sr_{1/3}CoO_{3-\delta}$ and $Nd_{1/3}Sr_{2/3}CoO_{3-\delta}$; (Figure S2) thermal evolution of the unit cell volume of $Nd_{2/3}Sr_{1/3}CoO_{3-\delta}$ and (b) $Nd_{1/3}Sr_{2/3}CoO_{3-\delta}$ in air; (Figure S3) NPD for $Nd_{1/3}Sr_{2/3}CoO_{3-\delta}$ at 1073 K in air (Figure S4); mass loss and oxygen loss a function of temperature for $Nd_{2/3}Sr_{1/3}CoO_{3-\delta}$ and $Nd_{1/3}Sr_{2/3}CoO_{3-\delta}$; (Table S1) nominal and experimental (determined by EDS) compositions for the $Nd_{2/3}Sr_{1/3}CoO_{3-\delta}$ sample used for NPD and electrical characterization; (Table S2) nominal and experimental (determined by EDS) compositions for the $Nd_{1/3}Sr_{2/3}CoO_{3-\delta}$ sample used for NPD and electrical characterization; (Table S3) structural parameters for $Nd_{1-x}Sr_xCoO_{3-\delta}$ obtained from joint fitting of NPD and PXRD data; (Table S4) selected structural information for $Nd_{1-x}Sr_xCoO_{3-\delta}$ (x = 1/3, 2/3) obtained from NPD data (PDF)

■ AUTHOR INFORMATION

Corresponding Authors

Daniel Muñoz-Gil − *Instituto de Cerámica y Vidrio, CSIC, Cantoblanco, 28049 Madrid, Spain;* orcid.org/0000-0002-0443-9008; Email: danielmg@icv.csic.es

Khalid Boulahya − *Departamento de Química Inorgánica, Facultad Ciencias Químicas, Universidad Complutense, E-28040 Madrid, Spain*; Email: khalid@ucm.es

Authors

M. Teresa Azcondo − *Departamento de Química y Bioquímica, Facultad de Farmacia, Universidad CEU San Pablo, E-28668 Madrid, Spain;* orcid.org/0000-0002-3890-0800

Clemens Ritter − *Institut Laue-Langevin, BP 156-38042 Grenoble, Cedex 9, France*

Oscar Fabelo − *Institut Laue-Langevin, BP 156-38042 Grenoble, Cedex 9, France;* orcid.org/0000-0001-6452-8830

Domingo Pérez-Coll − *Instituto de Cerámica y Vidrio, CSIC, Cantoblanco, 28049 Madrid, Spain;* orcid.org/0000-0001-5331-2516

Glenn C. Mather − *Instituto de Cerámica y Vidrio, CSIC, Cantoblanco, 28049 Madrid, Spain;* orcid.org/0000-0003-0779-4619

Ulises Amador − *Departamento de Química y Bioquímica, Facultad de Farmacia, Universidad CEU San Pablo, E-28668 Madrid, Spain;* orcid.org/0000-0002-4412-2419

Complete contact information is available at: https://pubs.acs.org/10.1021/acs.inorgchem.0c01049

Notes

The authors declare no competing financial interest.

■ ACKNOWLEDGMENTS

We thank MICINN for funding the projects MAT2016-78362-C4-1-R, MAT2016-78362-C4-4-R, and RTI2018-095088-B-I00 and ILL for allocation of beam time (experiment codes 5-24-583 and CRG-D1B-19-379; DOI: 10.5291/ILL-DATA.CRG-2713). The authors also thank the "Comunidad de Madrid" and European Structural Funds for their financial support of the MATERYENER3-CM (S2013/MIT-2753) project. We are also grateful to the "Red de Excelencia" (MINECO, MAT 2017-090695-REDT) for facilitating collaboration between the Spanish groups. U.A. and M.T.A. also thank USP-CEU for financial support.

■ REFERENCES

(1) Mitchell, R. H. *Perovskite: Modern and Ancient*; Almaz Press (Canada): Ontario, 2002.

(2) Zhu, L.; Ran, R.; Tadé, M.; Wang, W.; Shao, Z. Perovskite materials in energy storage and conversion. *Asia-Pac. J. Chem. Eng.* **2016**, *11*, 338−369.

(3) Jun, A.; Kim, J.; Shin, J.; Kim, G. Perovskite as a Cathode Material: A Review of its Role in Solid-Oxide Fuel Cell Technology. *ChemElectroChem* **2016**, 3, 511−530.

(4) Skinner, S. J. Recent advances in perovskite-type materials for SOFC cathodes. *Fuel Cells Bulletin* **2001**, *4*, 6−12.

(5) Tao, S. W.; Irvine, J. T. S. A Stable, Easily Sintered Proton-Conducting Oxide Electrolyte for Moderate-Temperature Fuel Cells and Electrolyzers. *Adv. Mater.* **2006**, *18*, 1581−1584.

(6) Gan, Y.; Zhang, J.; Li, Y.; Li, S.; Xie, K.; Irvine, J. Composite Oxygen Electrode Based on LSCM for Steam Electrolysis in a Proton Conducting Solid Oxide Electrolyzer. *J. Electrochem. Soc.* **2012**, *159*, F763−F767.

(7) Sunarso, J.; Baumann, S.; Serra, J. M.; Meulenberg, W. A.; Liu, S.; Lin, Y. S.; Diniz da Costa, J. C. Mixed ionic-electronic conducting (MIEC) ceramic-based membranes for oxygen separation. *J. Membr. Sci.* **2008**, *320*, 13−41.

(8) Huang, K.; Feng, M.; Goodenough, J. B.; Schmerling, M. Characterization of Sr-Doped $LaMnO_3$ and $LaCoO_3$ as Cathode Materials for a Doped $LaGaO_3$ Ceramic Fuel Cell. *J. Electrochem. Soc.* **1996**, *143*, 3630−3636.

(9) Huang, K.; Lee, H. Y.; Goodenough, J. B. Sr- and Ni-Doped $LaCoO_3$ and $LaFeO_3$ Perovskites: New Cathode Materials for Solid-Oxide Fuel Cells. *J. Electrochem. Soc.* **1998**, *145*, 3220−3227.

(10) Adler, S. B. Factors governing oxygen reduction in solid oxide fuel cell cathodes. *Chem. Rev.* **2004**, *104*, 4791−4843.

(11) Liu, Z.; Han, M.-F.; Miao, W.-T. Preparation and characterization of graded cathode $La_{0.6}Sr_{0.4}Co_{0.2}Fe_{0.8}O_{3-\delta}$. *J. Power Sources* **2007**, *173*, 837−841.

(12) Al Daroukh, M.; Vashook, V. V.; Ullmann, H.; Tietz, F.; Arual Raj, I. Oxides of the AMO_3 and A_2MO_4-type: structural stability, electrical conductivity and thermal expansion. *Solid State Ionics* **2003**, *158*, 141−150.

https://dx.doi.org/10.1021/acs.inorgchem.0c01049
Inorg. Chem. XXXX, XXX, XXX−XXX

(13) Amow, G.; Au, J.; Davidson, I. Synthesis and characterization of $La_4Ni_{3-x}Co_xO_{10\pm\delta}$ ($0.0 \le x \le 3.0$, $\Delta x = 0.2$) for solid oxide fuel cell cathodes. *Solid State Ionics* **2006**, *177*, 1837−1841.
(14) Azcondo, M. T.; Yuste, M.; Pérez-Flores, J. C.; Muñoz-Gil, D.; García-Martín, S.; Muñoz-Noval, A.; Orench, I. P.; García-Alvarado, F.; Amador, U. Defect Chemistry, Electrical Properties, and Evaluation of New Oxides $Sr_2CoNb_{1-x}Ti_xO_{6-\delta}$ ($0 \le x \le 1$) as Cathode Materials for Solid Oxide Fuel Cells. *ChemSusChem* **2017**, *10*, 2978−2989.
(15) Jennings, A. J.; Skinner, S. J. Thermal stability and conduction properties of the $La_xSr_{2-x}FeO_{4+\delta}$ system. *Solid State Ionics* **2002**, *152*, 663−667.
(16) Petrie, J. R.; Jeen, H.; Barron, S. C.; Meyer, T. L.; Lee, H. N. Enhancing Perovskite Electrocatalysis through Strain Tuning of the Oxygen Deficiency. *J. Am. Chem. Soc.* **2016**, *138*, 7252−7255.
(17) Hammouche, A. Electrocatalytic Properties and Nonstoichiometry of the High Temperature Air Electrode $La_{1-x}Sr_xMnO_3$. *J. Electrochem. Soc.* **1991**, *138*, 1212.
(18) Adler, S. B. Electrode Kinetics of Porous Mixed-Conducting Oxygen Electrodes. *J. Electrochem. Soc.* **1996**, *143*, 3554.
(19) Petrov, A. N.; Kononchuk, O. F.; Andreev, A. V.; Cherepanov, V. A.; Kofstad, P. Crystal structure, electrical and magnetic properties of $La_{1-x}Sr_xCoO_{3-y}$. *Solid State Ionics* **1995**, *80*, 189−199.
(20) Raveau, B., Seikh, M. *Cobalt Oxides: From Crystal Chemistry to Physics*; Wiley-VCH: Berlin, 2012.
(21) Deng, Z.-Q.; Zhang, G.-G.; Liu, W.; Peng, D.-k.; Chen, C.-s. Phase composition, oxidation state and electrical conductivity of $SrFe_{1.5-x}Co_xO_y$. *Solid State Ionics* **2002**, *152*−*153*, 735−739.
(22) Mayeshiba, T. T.; Morgan, D. D. Factors controlling oxygen migration barriers in perovskites. *Solid State Ionics* **2016**, *296*, 71−77.
(23) Jacobson, A. J. Materials for Solid Oxide Fuel Cells. *Chem. Mater.* **2010**, *22* (3), 660−674.
(24) Tsipis, E. V.; Kharton, V. V. Electrode materials and reaction mechanisms in solid oxide fuel cells: a brief review. *J. Solid State Electrochem.* **2008**, *12*, 1367−1391.
(25) Xia, C.; Rauch, W.; Chen, F.; Liu, M. $Sm_{0.5}Sr_{0.5}CoO_3$ cathodes for low-temperature SOFCs. *Solid State Ionics* **2002**, *149*, 11−19.
(26) Tu, H. Y.; Takeda, Y.; Imanishi, N.; Yamamoto, O. $Ln_{1-x}Sr_xCoO_3$ (Ln = Sm, Dy) for the electrode of solid oxide fuel cells. *Solid State Ionics* **1997**, *100*, 283−288.
(27) Lee, K. T.; Manthiram, A. Comparison of $Ln_{0.6}Sr_{0.4}CoO_{3-\delta}$ (Ln = La, Pr, Nd, Sm, and Gd) as Cathode Materials for Intermediate Temperature Solid Oxide Fuel Cells. *J. Electrochem. Soc.* **2006**, *153*, A794.
(28) Guo, Y. M.; Shi, H. G.; Ran, R.; Shao, Z. P. Performance of $SrSc_{0.2}Co_{0.8}O_{3-\delta}$ + $Sm_{0.5}Sr_{0.5}CoO_{3-\delta}$ mixed-conducting composite electrodes for oxygen reduction at intermediate temperatures. *Int. J. Hydrogen Energy* **2009**, *34*, 9496−9504.
(29) Koyama, M.; Wen, C. J.; Masuyama, T.; Otomo, J.; Fukunaga, H.; Yamada, K.; Eguchi, K.; Takahashi, H. The mechanism of porous $Sm_{0.5}Sr_{0.5}CoO_3$ cathodes used in solid oxide fuel cells. *J. Electrochem. Soc.* **2001**, *148*, A795−A801.
(30) Amsif, M.; Marrero-Lopez, D.; Ruiz-Morales, J. C.; Savvin, S. N.; Nunez, P. Effect of sintering aids on the conductivity of $BaCe_{0.9}Ln_{0.1}O_{3-\delta}$. *J. Power Sources* **2011**, *196*, 9154−9163.
(31) Rossignol, C.; Ralph, J. M.; Bae, J. M.; Vaughey, J. T. $Ln_{1-x}Sr_xCoO_3$ (Ln = Gd, Pr) as a cathode for intermediate-temperature solid oxide fuel cells. *Solid State Ionics* **2004**, *175*, 59−61.
(32) Orera, A.; Slater, P. R. New Chemical Systems for Solid Oxide Fuel Cells. *Chem. Mater.* **2010**, *22*, 675−690.
(33) Lee, K. T.; Manthiram, A. Characterization of $Nd_{1-x}Sr_xCoO_{3-\delta}$ ($0 \le x \le 0.5$) cathode materials for intermediate temperature SOFCs. *J. Electrochem. Soc.* **2005**, *152*, A197−A204.
(34) Yamamoto, O.; Takeda, Y.; Kanno, R.; Noda, M. Perovskite-type oxides as oxygen electrodes for high-temperature oxide fuel-cells. *Solid State Ionics* **1987**, *22*, 241−246.
(35) Choi, S.; Shin, J.; Ok, K. M.; Kim, G. Chemical compatibility, redox behavior, and electrochemical performance of $Nd_{1-x}Sr_xCoO_{3-\delta}$ cathodes based on $Ce_{1.9}Gd_{0.1}O_{1.95}$ for intermediate-temperature solid oxide fuel cells. *Electrochim. Acta* **2012**, *81*, 217−223.
(36) Rodríguez-Carvajal, J. Recent advances in magnetic structure determination by neutron powder diffraction. *Phys. B* **1993**, *192*, 55−69.
(37) Yuste, M.; Perez-Flores, J. C.; de Paz, J. R.; Azcondo, M. T.; Garcia-Alvarado, F.; Amador, U. New perovskite materials of the $La_{2-x}Sr_xCoTiO_6$ series. *Dalton Trans.* **2011**, *40*, 7908−7915.
(38) Johnson, J. *ZView: A software Program for IES Analysis*, version 2.9c; Scribner Associates Inc, 2005.
(39) Maupoey, Z.; Azcondo, M. T.; Pérez-Flores, J. C.; Ritter, C.; Boulahya, K.; Amador, U.; García-Alvarado, F. A-site substoichiometry and oxygen vacancies as the origin of the electrical properties of $Sr_{2-y}LuNb_{1-x}Ti_xO_{6-\delta}$ perovskite-like materials. *Dalton Trans.* **2014**, *43*, 14099.
(40) Shannon, R. Revised effective ionic radii and systematic studies of interatomic distances in halides and chalcogenides. *Acta Crystallogr., Sect. A: Cryst. Phys., Diffr., Theor. Gen. Crystallogr.* **1976**, *32*, 751−767.
(41) Glazer, A. The classification of tilted octahedra in perovskites. *Acta Crystallogr., Sect. B: Struct. Crystallogr. Cryst. Chem.* **1972**, *28*, 3384−3392.
(42) Gomez-Perez, A.; Hoelzel, M.; Munoz-Noval, A.; Garcia-Alvarado, F.; Amador, U. Effect of Internal Pressure and Temperature on Phase Transitions in Perovskite Oxides: The Case of the Solid Oxide Fuel Cell Cathode Materials of the $La_{2-x}Sr_xCoTiO_6$ Series. *Inorg. Chem.* **2016**, *55*, 12766−12774.
(43) Mountstevens, E. H.; Attfield, J. P.; Redfern, S. A. T. Cation-size control of structural phase transitions in tin perovskites. *J. Phys.: Condens. Matter* **2003**, *15*, 8315−8326.
(44) Zhao, J.; Ross, N. L.; Angel, R. J.; Carpenter, M. A.; Howard, C. J.; Pawlak, D. A.; Lukasiewicz, T. High-pressure crystallography of rhombohedral $PrAlO_3$ perovskite. *J. Phys.: Condens. Matter* **2009**, *21*, 235403.
(45) Khomchenko, V. A.; Troyanchuk, I. O.; Többens, D. M.; Sikolenko, V.; Paixão, J. A. Composition- and temperature-driven structural transitions in $Bi_{1-x}Ca_xFeO_3$ multiferroics: a neutron diffraction study. *J. Phys.: Condens. Matter* **2013**, *25*, 135902.
(46) Knight, K. S. Structural phase transitions, oxygen vacancy ordering and protonation in doped $BaCeO_3$: results from time-of-flight neutron powder diffraction investigations. *Solid State Ionics* **2001**, *145*, 275−294.
(47) Knee, C. S.; Magrasó, A.; Norby, T.; Smith, R. I. Structural transitions and conductivity of $BaPrO_3$ and $BaPr_{0.9}Y_{0.1}O_{3-\delta}$. *J. Mater. Chem.* **2009**, *19*, 3238−3247.
(48) Mather, G. C.; Heras-Juaristi, G.; Ritter, C.; Fuentes, R. O.; Chinelatto, A. L.; Pérez-Coll, D.; Amador, U. Phase Transitions, Chemical Expansion, and Deuteron Sites in the $BaZr_{0.7}Ce_{0.2}Y_{0.1}O_{3-\delta}$ Proton Conductor. *Chem. Mater.* **2016**, *28*, 4292−4299.
(49) Howard, C. J.; Knight, K. S.; Kennedy, B. J.; Kisi, E. H. The structural phase transitions in strontium zirconate revisited. *J. Phys.: Condens. Matter* **2000**, *12*, L677−L683.
(50) Zhang, L.; Li, X.; Zhang, L.; Cai, H.; Xu, J.; Wang, L.; Long, W. Improved thermal expansion and electrochemical performance of $La_{0.4}Sr_{0.6}Co_{0.9}Sb_{0.1}O_{3-\delta}$-$Ce_{0.8}Sm_{0.2}O_{1.9}$ composite cathode for IT-SOFCs. *Solid State Sci.* **2019**, *91*, 126−132.
(51) Fu, Y.-P. Electrochemical performance of $La_{0.9}Sr_{0.1}Co_{0.8}Ni_{0.2}O_{3-\delta}$-$Ce_{0.8}Sm_{0.2}O_{1.9}$ composite cathode for solid oxide fuel cells. *Int. J. Hydrogen Energy* **2011**, *36* (9), 5574−5580.
(52) Zhou, Q.; Wang, W.; Wei, T.; Qi, X.; Li, Y.; Zou, Y.; Liu, Y.; Li, Z.; Wu, Y. $LaBaCuFeO_{5+\delta}$-$Ce_{0.8}Sm_{0.2}O_{1.9}$ as composite cathode for solid oxide fuel cells. *Ceram. Int.* **2012**, *38* (2), 1529−1532.
(53) Zhou, Q.; Li, Y.; Shi, Y.; Zhang, X.; Wei, T.; Guo, S.; Huang, D. Electrochemical characterization of $LaBaCuCoO_{5+\delta}$-$Sm_{0.2}Ce_{0.8}O_{1.9}$ composite cathode for intermediate-temperature solid oxide fuel cells. *Mater. Res. Bull.* **2012**, *47* (1), 101−105.
(54) Zhou, Q.; Wang, F.; Shen, Y.; He, T. Performances of $LnBaCo_2O_{5+x}$-$Ce_{0.8}Sm_{0.2}O_{1.9}$ composite cathodes for intermediate-

https://dx.doi.org/10.1021/acs.inorgchem.0c01049
Inorg. Chem. XXXX, XXX, XXX−XXX

temperature solid oxide fuel cells. *J. Power Sources* **2010**, *195* (8), 2174−2181.
(55) Zapata-Ramírez, V.; et al. Enhanced Intermediate-Temperature Electrochemical Performance of Air Electrodes for Solid Oxide Cells with Spray-Pyrolyzed Active Layers. *ACS Appl. Mater. Interfaces* **2020**, *12*, 10571−10578.
(56) Napolsky, P. S.; Drozhzhin, O. A.; Istomin, S. Y.; Kazakov, S. M.; Antipov, E. V.; Galeeva, A. V.; Gippius, A. A.; Svensson, G.; Abakumov, A. M.; Van Tendeloo, G. Structure and high-temperature properties of the (Sr,Ca,Y)(Co,Mn)O_{3-y} perovskites-perspective cathode materials for IT-SOFC. *J. Solid State Chem.* **2012**, *192*, 186−194.
(57) Lengsdorf, R.; Ait-Tahar, M.; Saxena, S. S.; Ellerby, M.; Khomskii, D. I.; Micklitz, H.; Lorenz, T.; Abd-Elmeguid, M. M. Pressure-induced insulating state in (La,Sr)CoO_3. *Phys. Rev. B: Condens. Matter Mater. Phys.* **2004**, *69*, 140403.
(58) Kharton, V. V.; Kovalevsky, A. V.; Patrakeev, M. V.; Tsipis, E. V.; Viskup, A. P.; Kolotygin, V. A.; Yaremchenko, A. A.; Shaula, A. L.; Kiselev, E. A.; Waerenborgh, J. C. Oxygen Nonstoichiometry, Mixed Conductivity, and Mössbauer Spectra of $Ln_{0.5}A_{0.5}FeO_{3-\delta}$ (Ln = La-Sm, A = Sr, Ba): Effects of Cation Size. *Chem. Mater.* **2008**, *20*, 6457−6467.
(59) Fleig, J. Solid Oxide Fuel Cell Cathodes: Polarization Mechanisms and Modeling of the Electrochemical Performance. *Annu. Rev. Mater. Res.* **2003**, *33*, 361−382.
(60) Adler, S. B. Mechanism and kinetics of oxygen reduction on porous $La_{1-x}Sr_xCoO_{3-\delta}$ electrodes. *Solid State Ionics* **1998**, *111*, 125−134.
(61) Küngas, R.; Yu, A. S.; Levine, J.; Vohs, J. M.; Gorte, R. J. An Investigation of Oxygen Reduction Kinetics in LSF Electrodes. *J. Electrochem. Soc.* **2013**, *160*, F205−F211.
(62) Chen, Y.; Zhou, W.; Ding, D.; Liu, M.; Ciucci, F.; Tade, M.; Shao, Z. Advances in Cathode Materials for Solid Oxide Fuel Cells: Complex Oxides without Alkaline Earth Metal Elements. *Adv. Energy Mater.* **2015**, *5*, 1500537.
(63) Merkle, R.; Maier, J.; Bouwmeester, H. J. M. A linear free energy relationship for gas-solid interactions: Correlation between surface rate constant and diffusion coefficient of oxygen tracer exchange for electron-rich perovskites. *Angew. Chem., Int. Ed.* **2004**, *43*, 5069−5073.
(64) Merkle, R.; Maier, J. How Is Oxygen Incorporated into Oxides? A Comprehensive Kinetic Study of a Simple Solid-State Reaction with $SrTiO_3$ as a Model Material. *Angew. Chem., Int. Ed.* **2008**, *47*, 3874−3894.

https://dx.doi.org/10.1021/acs.inorgchem.0c01049
Inorg. Chem. XXXX, XXX, XXX−XXX